ARTICLE   OPEN

Check for updates

Frequency of the winter temperature extremes over Siberia dominated by the Atlantic Meridional Overturning Circulation

Huan Wang[1,2,3], Zhiyan Zuo[1,4,5 ✉], Liang Qiao[1,6], Kaiwen Zhang[1,6], Cheng Sun [7], Dong Xiao[8], Zouxing Lin[1], Lulei Bu[1] and Ruonan Zhang[1]

Widespread observed and projected increases in warm extremes, along with decreases in cold extremes, have been confirmed as being consistent with global and regional warming. Here we disclosed that the decadal variation in the frequency of the surface air temperature (SAT) extremes over Siberia in winter was primarily dominated by the Atlantic Meridional Overturning Circulation (AMOC) rather than anthropogenic forcing. The stronger AMOC induced more warm and cold extremes through increasing the variance of winter SAT over Siberia while the direct effect of external forcings, especially anthropogenic greenhouse gases, had little impact on the summation of warm and cold extremes due to equivalent effects on the increases in warm extremes and decreases in cold extremes. The possible mechanism can be deduced that the stronger AMOC stimulated the propagation of the wave train originated in the North Atlantic Ocean, across mid- to high latitudes, thereby increasing the variabilities in the circulations over the Ural blocking region and Siberia, which are critical to the SAT extremes there.

INTRODUCTION

A long-term increasing frequency of warm extremes and decreasing cold extremes were observed over Siberia during boreal winter along with global warming[1–4], and this tendency was projected to continue in the near future[5]. However, adverse cold winters over Siberia, concurrent with pronounced warming over the Arctic, known as the "warm Arctic cold Siberia (WACS)" pattern, have occurred in recent decades[6,7]. As a consequence, frequent severe winters, including persistent snow cover and cold extremes, occurred over Europe and Asia in 2005/2006[8], 2009/10[9,10], 2010/11[11], and most recently in 2020/21[12,13], making headlines in the major population centres of industrialized countries in the Northern Hemisphere.

Winter extremes have received major public attention due to their serious impacts on living creatures and ecosystems, as well as on human society. An open question that is critically important for scientists and policy-makers is whether any such increase in weather extremes is natural or anthropogenic in origin[14]. Anthropogenic global warming has been confirmed to be the dominant factor for the increases in intensity, frequency, and duration of warm extremes and the decrease in the likelihood of cold extremes[15]. However, changes in regional temperature extremes can be modulated by several factors other than anthropogenic influence and thereby show heterogeneous spatial distributions. The recent cold winters over mid- to high latitudes in the Northern Hemisphere, which unexpectedly interrupted the anthropogenic forcing-induced global warming trend, imply an internal mode of winter temperature variation[15,16]. Some suggest that the internal variability from the Atlantic Ocean may have dampened the magnitude of global warming over the historical era[16–18]. Anomalous surface heat fluxes released into the atmosphere caused by the Atlantic Meridional Overturning Circulation (AMOC) are critical for the climate over mid- to high latitudes in the Northern Hemisphere[19–24]. On the other hand, the AMOC-induced northwards flow of warm salty water in the upper Atlantic is a major source of substantial northwards Atlantic heat transport[25]. Northwards heat transportation strongly affects the sea ice distribution[20,26,27] and, since the late 1990s, presumably has been linked to Arctic amplification (AA)[27,28]. These results make us wonder if AMOC can directly affect the surface air temperature (SAT) extremes over Siberia in winter.

Most previous studies have focused on the causes of a specific extreme event or short-term behaviours of regional SAT extremes instead of their decadal-scale variations, and the dominant factor for these extremes has not been clearly established[29,30]. In this study, we examine the frequencies of the winter SAT extremes over Siberia and explore the dominant effect of AMOC on their decadal variations utilizing observational and reanalysis datasets combining climate model simulations. The findings will shed light on the AMOC effect on SAT variability and deepen our understanding of the interactive influences of natural variability and anthropogenic forcing on climate change.

RESULTS

Decadal variation in the winter SAT extremes over Siberia dominated by AMOC

Robust relationship between AMOC and the frequency of the winter SAT extremes over Siberia. We examined the frequency histogram and conducted a normal Gaussian distribution fitting (GDF) of the winter SAT anomalies (daily SATs minus winter SAT mean during 1960–2017) over Siberia (50°−70°N, 60°−120°E) based on the

[1]Department of Atmospheric and Oceanic Sciences/Institute of Atmospheric Sciences, Fudan University, Shanghai 200438, China. [2]College of Geography and Resources Science, Sichuan Normal University, Chengdu 610101, China. [3]CMA-FDU Joint Laboratory of Marine Meteorology, Shanghai 200438, China. [4]National Observations and Research Station for Wetland Ecosystems of the Yangtze Estuary, Shanghai 202183, China. [5]Shanghai Frontiers Science Center of Atmosphere-Ocean Interaction, Shanghai 200123, China. [6]Chinese Academy of Meteorological Sciences, China Meteorological Administration, Beijing 100081, China. [7]College of Global Change and Earth System Science, Beijing Normal University, Beijing 100875, China. [8]Key Laboratory of Cites' Mitigation and Adaptation to Climate Change in Shanghai, China Meteorological Administration, Shanghai 200030, China. ✉email: zuozhy@fudan.edu.cn
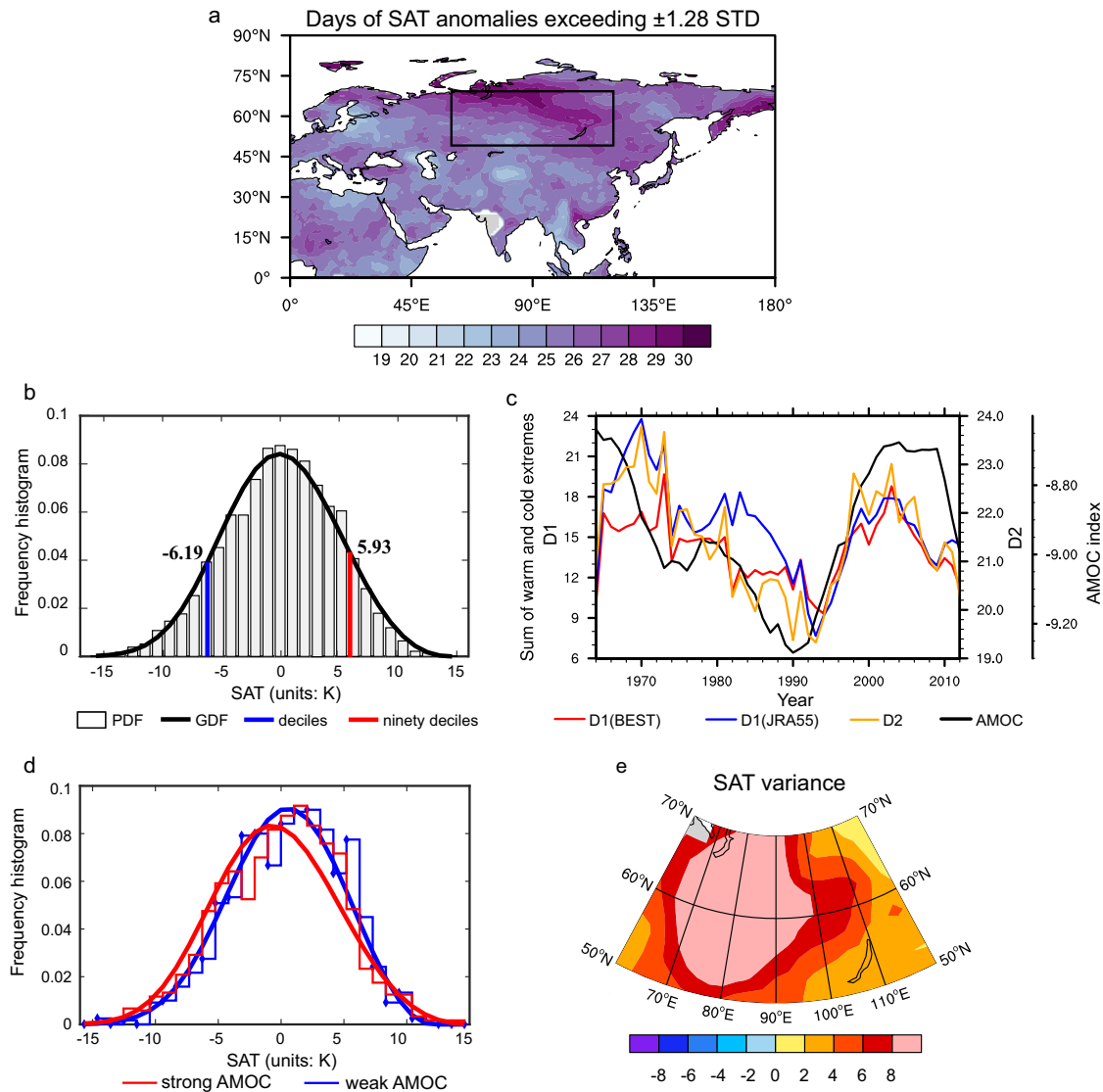
Fig. 1 Spatial and temporal characteristics of the winter SAT extremes over Siberia and their relationship with AMOC. a Spatial distribution of the Sums for the days (units: days season^{-1}) with the SAT anomaly either greater than its 1.28 STD or less than −1.28 STD in winter during 1960–2016; the black box is the Siberian region. **b** Frequency histogram (bars) and GDF fitting (curve) of the winter SAT anomalies (units: K) over Siberia during 1960–2016. **c** Decadal changes in the frequencies (days season^{-1}) for the Sums over Siberia in winter based on D1 using the BEST and JRA55 datasets and D2 and the fingerprint AMOC index during 1960–2016 (the year 1964 represents the 9 years' moving average from 1960 to 1968). **d** Frequency histograms (staircase curves) and GEV fittings (smooth curves) of the winter SAT anomalies (units: K) over Siberia during the weak AMOC (blue lines) and strong AMOC phases (red lines). **e** Differences in the variances (unit: K^2) of the winter SATs over Siberia between the strong and weak AMOC phases. The SAT anomalies in **a**, **b**, **d**, and **e** are from the BEST dataset.

Berkeley Earth Surface Temperature (BEST) dataset (details in "Methods"). An essential Gaussian distribution (passing the Jarque-Bera Test[31]) is shown in Fig. 1b, where the 90th percentile (5.93 K) and the 10th percentile (−6.19 K) of this distribution are nearly symmetric and approximately equal to ±1.28 standard deviation (STD). If we count the days with winter SAT anomalies greater than 1.28 STD and less than −1.28 STD during 1960–2017 and calculate their summation at each grid (Fig. 1a), the greatest variation (more than 25 days in the 58 years) occurred over Siberia, making our study on the causes of the SAT extremes over this region particularly important.

Classical SAT extremes are described by the Expert Team on Climate Change Detection and Indices (ETCCDI)[32]. Since the SAT anomalies present an essential Gaussian distribution (Fig. 1b), a new definition was developed based on the ETCCDI procedure but aimed specifically at regional consistencies. For the Siberian region, if there are sufficient grids with daily SAT anomalies above (below) a certain multiple of their STD, an extreme warm (cold) day is identified (hereafter D1, for details, see "Methods").

The decadal variation (9-year moving average) in the sums of the frequencies for warm and cold extremes (hereafter Sums) over Siberia in winter based on D1 indicates an overall decreasing trend of ~5 days/season per decade from the beginning of the 1970s to the early 1990s, followed by a rapid increasing tendency of ~9 days/season per decade from the early 1990s to the early 2000s and a decrease to ~9 days/season per decade thereafter (Fig. 1c). This variation coincides with the fingerprint of the AMOC index (details in "Methods") with a correlation coefficient of 0.53 (significant at the 99% confidence level). Another subpolar upper ocean salinity index of AMOC (referred to AMOC (so) index hereinafter, details in "Methods") shows strong correlations with the fingerprint AMOC index (Supplementary Figure 1 and

Supplementary Table 1), implying that the AMOC index will not affect the results.

In addition, decadal changes in Sums based on the ETCCDI (hereafter D2) and different datasets were examined (Fig. 1c). Variations for D2 and D1 are fairly consistent with their correlation coefficient of 0.93 (significant at the 99% confidence level), confirming the fidelity of D1 in representing the SAT extremes, although the maximum changing amplitude of D1 is greater than D2 (~3.5 days/season per decade). Moreover, another 6-hourly SAT dataset of the Japanese 55-year Reanalysis (JRA55) from the Japan Meteorological Agency[33] was utilized as a complement. We first examine the correspondence between the SATs from the BEST data and the JRA55 reanalysis at a daily scale by combining the 120 days in winter of the 57 years (1960–2016) into a sequence (see Supplementary Figure 2). They display alignment on the daily scale with a correlation coefficient of 0.73, and their standard deviations for BEST and JRA55 are 4.72 and 4.71, respectively. These results guarantee the following JRA55-based physical mechanisms of the AMOC effect on the BEST-based SAT extremes over Siberia, which makes sense. Decadal variation in the Sums based on the JRA55 resembles the BEST with a correlation coefficient of 0.79 (significant at the 99% level), although the maximum changing amplitude of the JRA55 is even greater (~13 days/season per decade). In conclusion, neither the definitions of the SAT extremes and AMOC nor the datasets affect the robust relationship between the decadal change in AMOC and the frequencies of the winter SAT extremes over Siberia.

AMOC modulation of the winter SAT variance over Siberia. Based on to the decadal changes in AMOC in Fig. 1c, two decadal time frames of the weak AMOC (1985–1994) and the strong AMOC (1964–1968 combined with 1995–1999) were selected for comparison. The influence of the strong AMOC after 2000, when the prominent AA effect emerged, is analysed in the discussion section, as the AA effect gives rise to more SAT extremes over Siberia in a different physical mechanism. The frequency histograms of the regional averaged winter SAT anomalies over Siberia during the strong and weak AMOC phases based on the BEST datasets were used to analyse the AMOC effect on the SAT variances (Fig. 1d). The shapes of the frequency histograms resemble Gaussian distributions, and generalized extreme value (GEV) fittings generated by the Fischer-Tippett Theorem[34] were applied to better characterize the frequencies of the SAT extremes as the upper or lower PDF tails[35,36]. The scale parameters, which can determine the "steepness" of the GEV fitting (the smaller the scale parameter is, the steeper the curve), are 4.79 and 4.53 for the strong and weak AMOC phases, respectively. The GEV tails for the strong AMOC phase, on behalf of the warm and cold extremes, lie above those for the weak AMOC phase. These results imply that the greater SAT variance (flattened GEV shape) aggravated by the strong AMOC favours an increase in the Sum. In addition, we diagnosed the regional differences in the SAT variances over Siberia between the strong and weak AMOC. The spatial pattern in Fig. 1e presents positive anomalies over the whole Siberian region, and the changing amplitude exceeds 8 K^2 over western Siberia, further confirming the AMOC effect on the SAT variances.

CMIP6 simulations on the effects of external forcings on the SAT extremes over Siberia

The state-of-the-art Coupled Model Intercomparison Project, Phase 6 (CMIP6) of the World Climate Research Program (WCRP) models (details in "Methods") have been confirmed by previous studies as being able to capture the global surface temperature
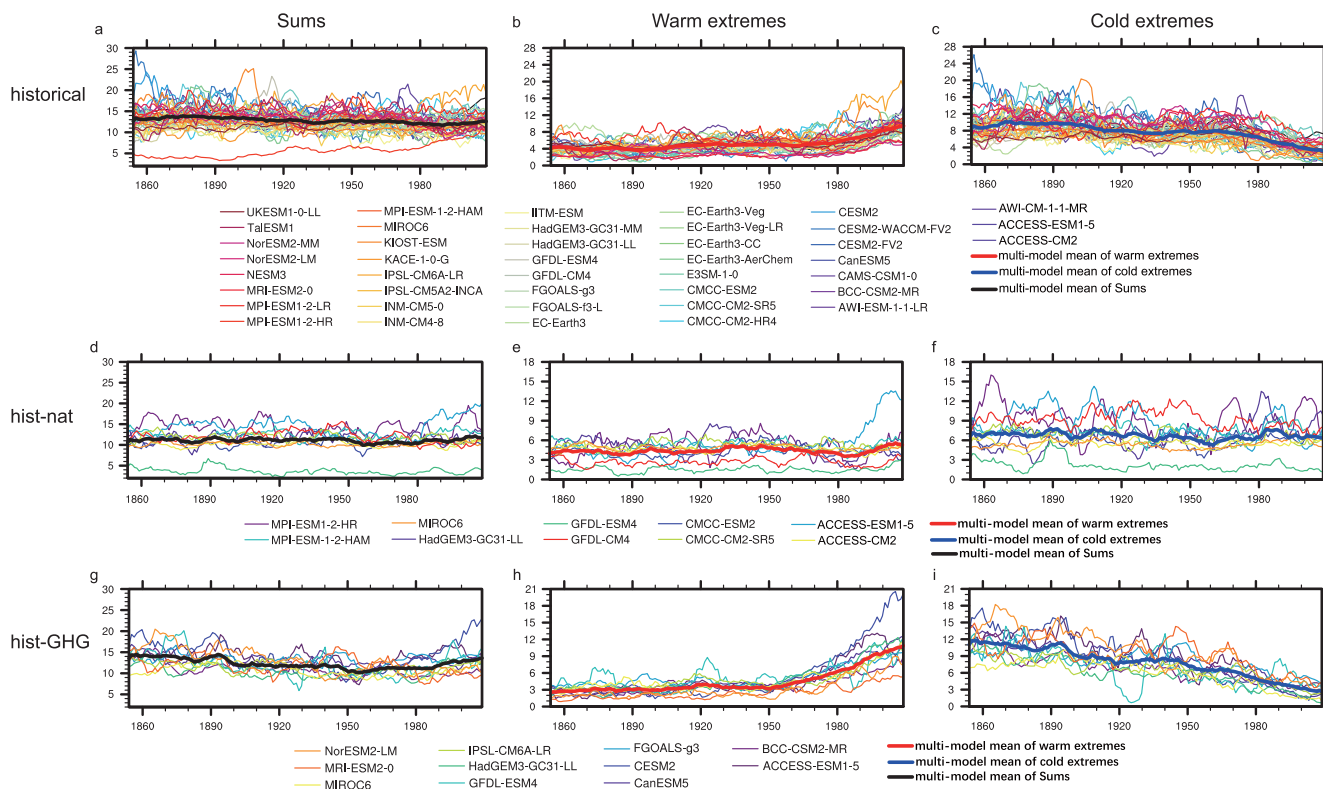

Fig. 2 Decadal variations in the SAT extremes over Siberia in winter based on the CMIP6 simulations. a Decadal variations in the Sums (**a, d, g**), warm extremes (**b, e, h**) and cold extremes (**c, f, i**) over Siberia in winter during 1850–2014 based on D1 (units: days season^{-1}) for each model in the historical (**a, b, c**), hist-nat (**d, e, f**) and hist-GHG runs (**g, h, i**). The black, red and blue thick lines are the multi-model means of the Sums, warm extremes and cold extremes, respectively. The x-axes are for years, and the y-axes are for the frequencies of the Sums, warm extremes and cold extremes (units: days season^{-1}).

distribution tail shape; thus, the model utility in temperature extremes is confident[37]. In this study, the frequency histograms of the daily SAT anomalies over Siberia in winter during 1850–2014 resemble Gaussian distributions (r1i1p1f1 members of 6 models in the historical experiment as examples; see Supplementary Figure 3), confirming the fidelity to discuss the SAT extremes in models.

The Sixth Assessment Report (AR6) of the Intergovernmental Panel on Climate Change (IPCC) has concluded that anthropogenic global warming is the dominant factor influencing the increase in warm extremes and decrease in the likelihood of cold extremes[15]. However, we raised the point that the decadal change in the Sum over Siberia in wintertime is not the consequence of anthropogenic forcings. Since the internal variations among individual realizations are usually uncorrelated and thus are averaged out over a large number of ensemble members, the multi-model mean from the large CMIP6 ensembles contains mostly external forcing changes[38,39]. The response of the SAT extremes to the variations in all external forcings, natural external forcings, and anthropogenic greenhouse gases forcings were estimated by the multi-model means of the historical runs, hist-nat runs, and hist-GHG runs, respectively (details in "Methods"). All the decadal variations in the Sums over Siberia based on D1 for the multi-model means of the historical runs (Fig. 2a), hist-nat runs (Fig. 2d) and hist-GHG runs (Fig. 2g) present feeble amplitudes of less than 3 days/season per decade in the 165 years analysed. However, the underlying reasons for the faint changes are different. For the hist-nat experiment, natural external forcings

can influence neither warm extremes (Fig. 2e) nor cold extremes (Fig. 2f). However, for the historical (Fig. 2b, c) and hist-GHG experiments (Fig. 2h, i), all external forcings and anthropogenic greenhouse gases have relatively equivalent effects on the increase in warm extremes (Fig. 2b, h) and the decrease in cold extremes (Fig. 2c, i). Nevertheless, the feeble variations in the multi-model means of the Sums suggest that neither natural external forcings nor anthropogenic greenhouse gases can distinctly impact the decadal change in the frequencies of the Sums over Siberia.

CMIP6 simulations of the AMOC effect on the winter SAT extremes over Siberia

Considering the small impact of external forcings on the Sums and the robust relationship between AMOC and the winter SAT extremes over Siberia in the observation, another CMIP6 hist-resAMO experiment was utilized to examine whether the relationship exists in model simulations. The hist-resAMO experiment is a pacemaker-coupled historical climate simulation but with SST restored to the model climatology plus an observational historical anomaly in the AMO domain (details in "Methods"). Previous studies have demonstrated that AMO is primarily associated with internal variability associated with AMOC in reanalysis and model simulations[19,40,41]; thus, we assume that this experiment clarifies the AMOC signal more than the historical one. The frequency histograms of the daily SAT anomalies over Siberia in winter during 1870–2014 based on the hist-resAMO runs show
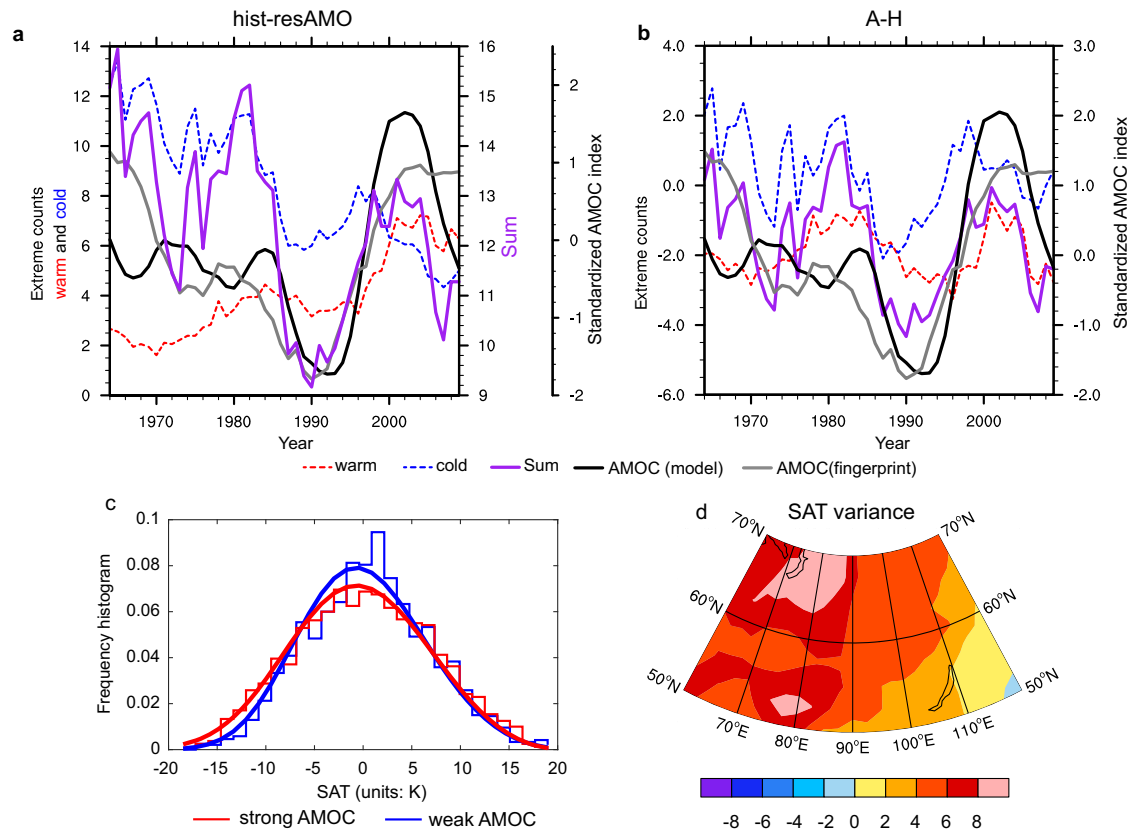

Fig. 3 AMOC effect on the winter SAT extremes over Siberia based on the model simulations. Decadal changes in the frequencies (day season^{-1}) of warm extremes (dashed red line), cold extremes (dashed blue line) and Sums (solid purple line) over Siberia in winter and the AMOC (so) index (solid black line) during 1960–2016 based on the multi-model means of the hist-resAMO experiment (**a**) and A-H experiment (**b**). The fingerprint AMOC index (solid grey line) is shown for comparison. The left y-axis is for warm and cold extremes, and the right two y-axes are for the Sum and AMOC index in (**a**). The left y-axis is for warm, cold extremes and Sum, and the right y-axis is for the AMOC index in (**b**). **c** Frequency histograms (staircase curves) and GEV fittings (smooth curves) of the winter SAT anomalies (unit: K) over Siberia during the weak AMOC phase (blue lines) and strong AMOC phase (red lines). **d** Differences in the variances (unit: K^2) of the winter SATs over Siberia between the strong and weak AMOC phases. **c** and **d** are based on the multi-model composite of the hist-resAMO runs.
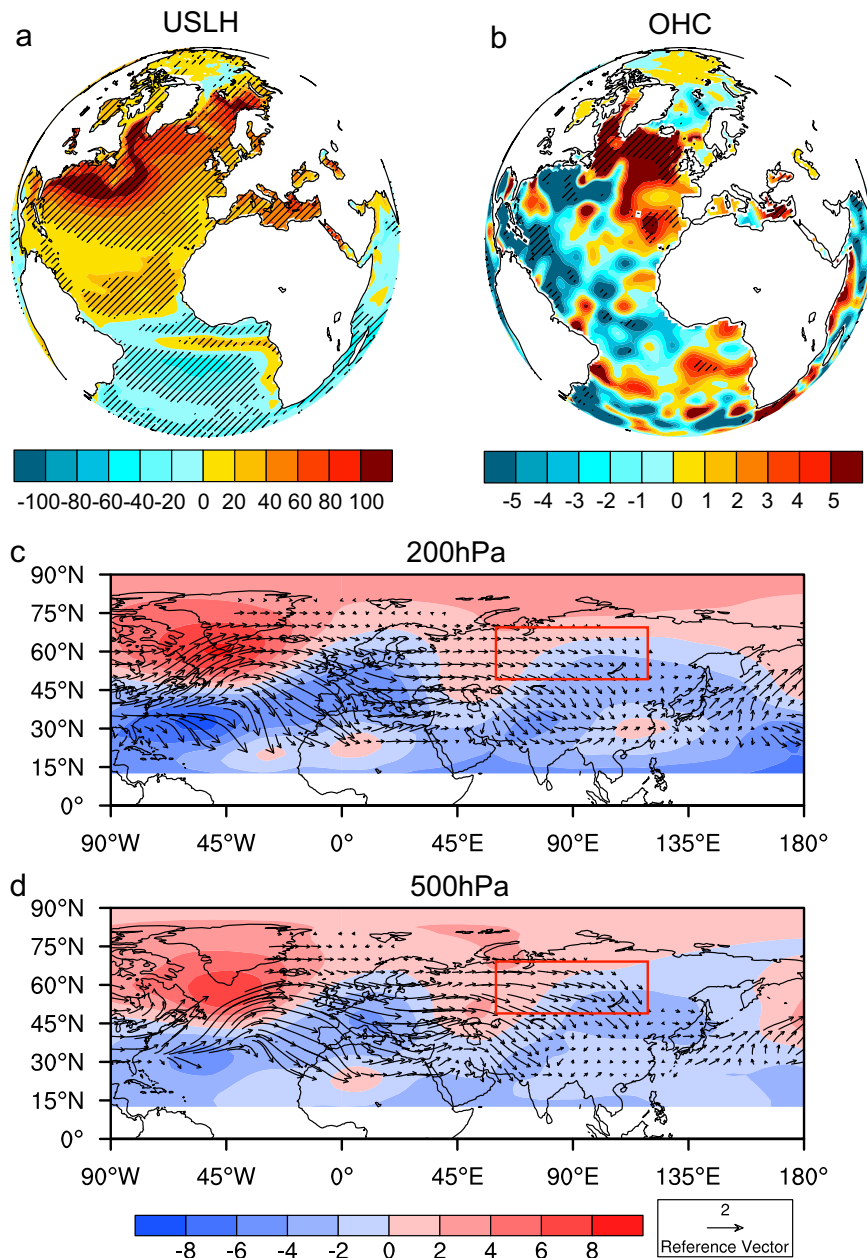
Fig. 4 Differences in the sea-air heat exchange and ocean heat transmission in winter between the strong and weak AMOC phases. Difference in the **a** USLH (shadings, units: W·m^{-2}, based on the WHOI dataset), **b** 0–700 m OHC (shadings, units: 10^{18} joules, based on the NECI dataset) and stream functions (shadings, units: m^2·s^{-1}) and wave activity fluxes (vectors, units: m^2·s^{-2}) at 200 hPa (**c**) and 500 hPa (**d**) based on the NECP datasets in winter between the strong and weak AMOC phases. Hatched areas in **a** and **b** indicate significance at the 95% confidence level using Student's t test for USLH and OHC, respectively. The red boxes in **c** and **d** are the Siberia region.

approximate Gaussian distributions as well (Supplementary Figure 4), which guarantees the following analyses.

The AMOC signals defined by the maximum Atlantic meridional overturning stream function (hereafter max AMOC index, details in "Methods") were applied to diagnose model abilities in simulating the mean state of AMOC during 1870–2014 (details in Supplementary Figure 5). The depths of the max AMOC cell at 27.5°N of the hist-resAMO models are all below 1 km, which is consistent with the RAPID observational result (mooring array deployed in 2004 off the coast of Florida to monitor AMOC[42]). However, the historical experiment and BCC-CSM2-MR model in the hist-resAMO experiment cannot simulate AMOC reasonably (details in Supplementary Figures 5, 6)[43,44]. Therefore, the following analysis is based on the FIO-ESM-2-0 and MRI-ESM2-0 models due to their good consistency and better approximation of the AMOC intensity to the RAPID observation.

Figure 3a depicts reasonably synchronous characteristics of the decadal variations in both the warm and cold extremes and their summations with AMOC (both the AMOC (so) index in the hist-resAMO models and the fingerprint AMOC index). This substantiates the observations in Fig. 1d that a strong AMOC increases the SAT variance and induces both warm and cold extremes. The long-term increasing trend in warm extremes and decreasing trend in cold extremes can be induced by external forcings. To focus on the AMOC effect only, we used the data in Fig. 3b to conduct an A-H (hist-resAMO minus historical) experiment in which the multi-model means of the SAT extremes in the historical experiment were subtracted from the corresponding extremes of
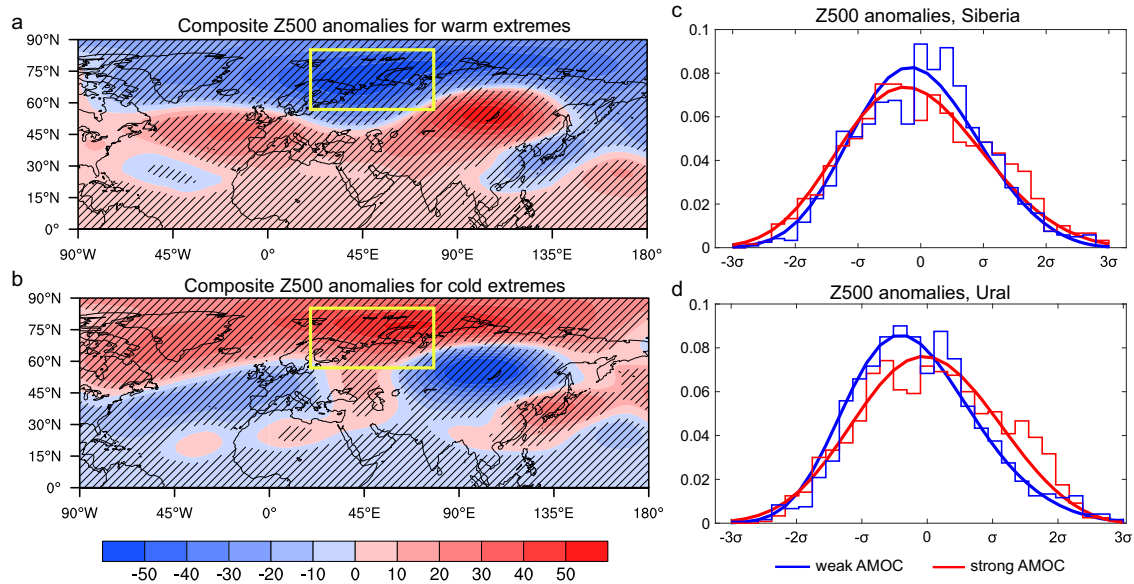
Fig. 5 A possible mechanism of the AMOC effect on atmospheric circulations. Composition of the daily Z500 anomalies (units: gpm) when warm (**a**) and cold (**b**) extremes occur over Siberia. Hatched areas indicate significance at the 95% confidence level using Student's t test. The yellow boxes in **a** and **b** are the Ural blocking region. Frequency histograms (staircase curves) and GEV fittings (smooth curves) of the Z500 anomalies over Siberia (**c**) and the Ural blocking region (**d**) during the weak AMOC phase (blue lines) and strong AMOC phase (red lines). The x-axes in **c** and **d** are the standard deviations (σ, units: K) of the daily Z500 anomalies, and the y-axes are the frequency histograms. All Z500 values are based on the JRA55 dataset.

the multi-model means in the hist-resAMO experiment. The variations in warm extremes, cold extremes and their summations without trends resemble AMOC more than Fig. 3a, further consolidating the argument that AMOC modulates the winter SAT extremes over Siberia.

Moreover, the frequency histogram of the winter SAT over Siberia during different AMOC phases was examined based on the hist-resAMO runs. Strong and weak AMOC phases are 1991–2000 and 1976–1985 for the FIO-ESM-2-0 model and 1979–1988 and 1989–1998 for the MRI-ESM2-0 model, respectively. The multi-model composite of the hist-resAMO runs (Fig. 3c) resembles a Gaussian distribution as well. Similar to the observations, the stronger AMOC flattens the GEV with scale parameters of 6.98 and 6.19 for the strong and weak AMOC phases, respectively. Both tails of the GEV for the strong AMOC phase lie above those for the weak AMOC, indicating more warm and cold extremes and therefore more Sums. The spatial pattern of the SAT variances over Siberia for the multi-model composite of the hist-resAMO runs in Fig. 3d also resembles the observation, with the largest variances occurring in western Siberia. In terms of each model in the hist-resAMO experiment (Supplementary Figure 7), there are some differences, but they cannot influence the conclusion that the strong AMOC favours more winter SAT extremes over Siberia by increasing the SAT variances.

Physical mechanism of the AMOC effect on the winter SAT extremes over Siberia

Sea-air energy exchange and transmission induced by AMOC. Figure 4 shows the differences in the sea-air energy exchange and transmission in winter between the composition of the strong and weak AMOC phases (the phases are consistent with Fig. 1d). Both the upwards surface sensible and latent heat (hereafter referred to as USLH, Fig. 4a) provided by the Woods Hole Oceanographic Institution (WHOI) Objectively Analysed air-sea Fluxes (OAFlux) for the Global Oceans (details in "Methods") and the 0–700 m ocean heat content (OHC, Fig. 4b) derived from the NOAA National Centers for Environmental Information (NCEI) world ocean heat content dataset (details in "Methods") manifest

positive anomalies between the strong and weak AMOC phases, meaning that the strong AMOC releases more surface heat fluxes into the atmosphere and transports additional meridional heat from the tropical to higher latitudes through the subsurface Atlantic Ocean. This heat release and transportation were confirmed to be critical for the climate over mid- to high latitudes in the Northern Hemisphere[19–21,25–28,45].

In addition, steam functions and wave activity fluxes defined by Takaya and Nakamura[46] were calculated utilizing the monthly fields of the horizontal wind velocities and monthly means of the daily geopotential heights at 200 hPa (hereafter Z200, Fig. 4c) and 500 hPa (hereafter Z500, Fig. 4d) from the National Centers for Environmental Prediction/National Center for Atmospheric Research (NCEP) reanalysis datasets (details in "Methods") and the JRA55 reanalysis datasets (see Supplementary Figure 8). There are significant wave trains originating from the subtropical North Atlantic Ocean and propagating across mid- to high latitudes towards Siberia both in the upper (Fig. 4c and Supplementary Figure 8a) and middle troposphere (Fig. 4d and Supplementary Figure 8b), implying that the wave trains initiated by the stronger AMOC will modulate the downstream atmospheric circulations and climate.

AMOC modulation of the atmospheric circulations over the Ural blocking region and Siberia. The composition of the daily Z500 anomalies when warm extremes occur over Siberia (Fig. 5a based on the JRA55 datasets and Supplementary Figure 9a based on the NCEP datasets) demonstrates a pronounced Atlantic-Eurasian wave train pattern across mid- to high latitudes, connecting a high-pressure centre over west Europe, a prominent low-pressure (less than −50 gpm) centre over the Ural region (55°–85°N, 20°–80°E) and very strong high-pressure centre (greater than 50 gpm) over Siberia. The negative anomalies at high latitudes (north to 65°N) across a wide range from 90°W to 180°E indicate that the polar vortex is strong enough to constrain cold air in the Arctic. In contrast, when cold extremes occur over Siberia (Fig. 5b and Supplementary Figure 9b), the pronounced Atlantic-Eurasian wave train pattern connects a significant high centre over the Ural
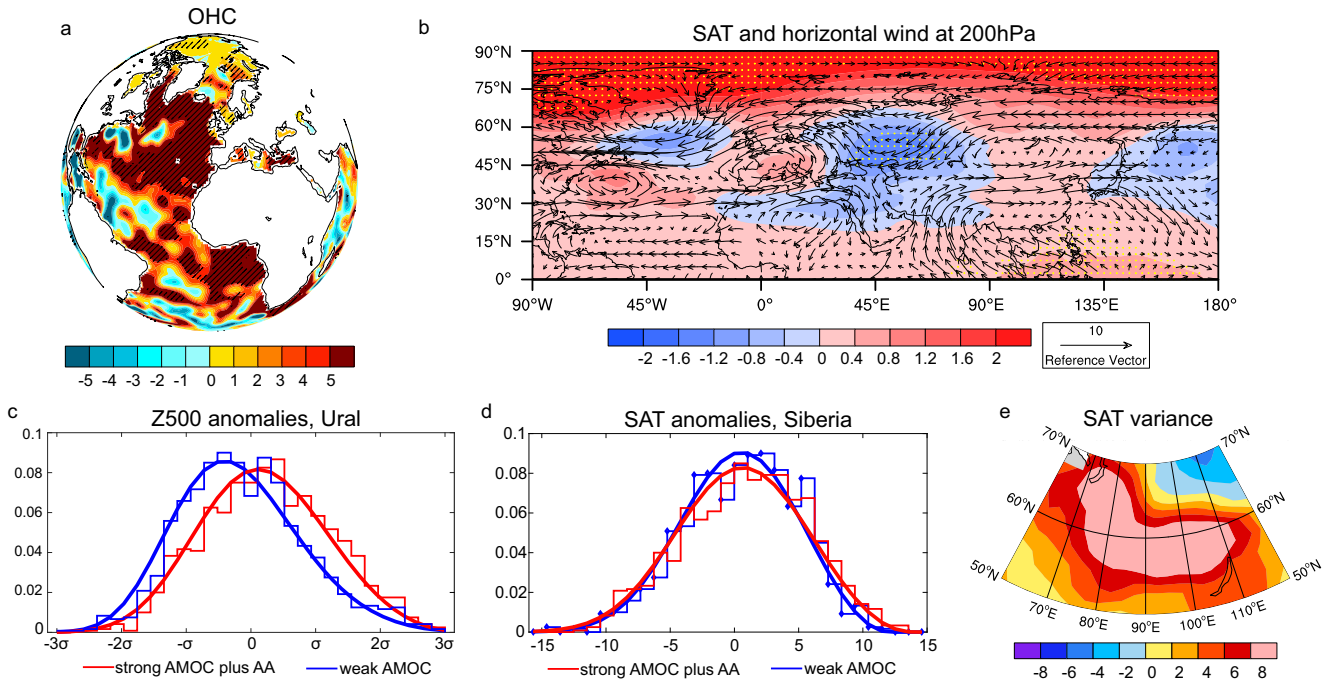
Fig. 6 A possible mechanism of the AMOC combined with the AA effect on the winter SAT extremes over Siberia. Difference in the **a** 0–700 m OHC (units: 10^{18} joules, based on the NCEI dataset) and **b** SAT (shadings, units: K) and horizontal wind at 200 hPa (vectors, units: $m \cdot s^{-1}$) in winter between the strong AMOC plus AA phase and the weak AMOC phase based on the JRA55 datasets. Hatched areas in **a** and yellow dots in **b** indicate significance at the 95% confidence level using Student's t test for the variation in OHC and SAT, respectively. Frequency histograms (staircase curves) and GEV fittings (smooth curves) of the Z500 anomalies (units: gpm) over the Ural blocking region (**c**, based on the JRA55 datasets) and the winter SATs (units: K) over Siberia (**d**, based on the BEST datasets) during the weak AMOC phase (blue lines) and strong AMOC plus AA phase (red lines). The x-axes are for the standard deviations (σ, unit: K) of the daily Z500 anomalies in (**c**) and SAT anomalies in (**d**), and the y-axes are for the frequency histograms. **e** Differences in the variances of the winter SATs (unit: K^2, based on the BEST dataset) over Siberia between the strong AMOC plus AA and weak AMOC phases.

region (more than 50 gpm) and a low centre (less than −50 gpm) over Siberia. Many previous studies[47–50] have verified that the weakened polar vortex (represented by the positive Z500 anomalies at high latitudes in Fig. 5b) favours enhanced Ural blocking and leads to more widespread cold extremes downstream.

The Atlantic-Eurasian wave trains of the daily Z500 anomalies when SAT extremes occur over Siberia (Fig. 5a, b) are quite similar to Fig. 4d, indicating the AMOC effect on the atmospheric circulations over the Ural and Siberia regions. Thus, variabilities in the regional averaged Z500 anomalies over Siberia were examined based on the strong and weak AMOC phases. Figure 5c (based on the JRA55 datasets) and Supplementary Figure 9c (based on the NCEP datasets) demonstrate more extreme distributions of Z500 anomalies during the strong AMOC, where the two tails (greater than 1.2σ and less than −1.1σ) of the GEV line are both above those of the weak AMOC. In addition, extreme Ural blockings that generate SAT variability are associated with extreme events in many regions[51], including Europe[50,52], Eurasia[47], and Asia[53,54]. We examined the AMOC effect on the variability in regional mean Z500 over the Ural blocking region, as it is presumably linked to the wave train stimulated by AMOC. The result is shown in Fig. 5d (based on the JRA55 datasets) and Supplementary Figure 9d (based on the NCEP datasets). A more extreme distribution during the strong AMOC phase, where the two tails (greater than 0.5σ and less than -2σ) of the GEV fitting are both above those of the weak AMOC, indicates that the strong AMOC favours more extreme Ural Z500 variability. Combined with the results of Fig. 5a, b and Fig. 4d, the greater variabilities in Z500 anomalies over Siberia and the Ural blocking region due to the strong AMOC are conducive to both warm and cold extremes over Siberia.

DISCUSSION
Recent work showed that a weakened AMOC could explain a reduced Arctic sea ice loss in all seasons and cause the Northern Hemisphere midlatitude jets to move poleward[22]. In other words, a strengthened/weakened AMOC may enhance/diminish the Arctic amplification (AA) effect and thus influence the climate over mid- to high latitudes[20]. The AA effect emerged with intensity in the 2000s (Supplementary Figure 10); hence, we analysed the difference in the OHC between a strong AMOC phase accompanied by the AA effect during 2000–2009 (hereafter referred to as the strong AMOC plus AA phase) and a weak AMOC phase (Fig. 6a). There are significant positive anomalies over the whole Atlantic Ocean and even the Barents Sea, the region in which the AA is most dominant[55], meaning that additional heat from the North Atlantic Ocean has been transported even further into the Arctic and strengthened AA since 2000. AA reduces the temperature gradient from the mid- to high latitudes to the North Pole in the whole Northern Hemisphere and weakens the upper-level jet stream (Fig. 6b and Supplementary Figure 11a). Compared with the weak AMOC, the strong AMOC plus AA enhances the Ural blockings by shifting the frequency distribution of the Z500 anomalies towards the positive direction (Fig. 6c and Supplementary Figure 11b). Thus, more cold air from the Arctic is transported into the relatively low latitudes and entails an increasing probability of cold extremes over Siberia. This mechanism has already been confirmed by previous studies[9,56–59]. In conjunction with the increases in warm extremes due to global warming, a more extreme distribution of the SAT anomalies (Fig. 6d) is manifested with more SAT variance over Siberia (Fig. 6e) during the strong AMOC plus AA phase. As a result, more SAT extremes have occurred over Siberia since 2000.

The physical mechanism of the AMOC effect on the winter SAT extremes over Siberia was preliminarily explored in this study. More mechanisms found by previous studies can be summarized in thermal and dynamic ways. In terms of the thermal effects, the upper branch of the AMOC can transport warm water and excess ocean heat from tropical regions to the mid- to high latitudes of the North Atlantic. This process is like the "Achilles heel" of the global climate system. Once it weakens or even collapses, less heat is transferred to the high latitudes. The cooling first occurs in Western Europe and North America, which are closest to the North Atlantic, and then occurs throughout the entire Northern Hemisphere[22,23]. The AMOC suddenly weakened occurred ~12,800 years ago and halted global warming, with the global average temperature dropping by ~6 °C. The whole event lasted ~1200 years and is known as the Younger Dryas event[60]. In other words, the thermal effect of the stronger AMOC can warm Siberia and contribute to more warm extremes there.

On the other hand, AMOC modulates the downstream climate in a dynamic way. The warm water brought by the North Atlantic Current penetrates into the Arctic region to strengthen the AA. The AMOC variation is significantly anticorrelated with the Arctic sea ice extent anomalies and correlated with the Arctic SAT anomalies on decadal time scales in the Atlantic sector of the Arctic[20]. Then, cold air masses such as the Arctic vortex that originally swirled over the Arctic region are driven towards Siberia and finally aggravate the occurrence of the SAT extremes there[24].

However, the intrinsic physical mechanism of the AMOC effect on SAT extremes cannot be easily divided into thermal or dynamic effects in the real world and depends on the research region. For example, Western Europe and North America may be more affected by the thermal effect as they are close to the North Atlantic. While Siberia may be more influenced by the dynamic mechanism discussed in our study, the wave train originating from the North Atlantic Ocean across the mid- to high latitudes contributes to more extreme atmospheric circulations over the Ural and Siberian regions. Nevertheless, further studies concerning the AMOC effect on ocean-air energy budget, large-scale air circulation, and local thermodynamic anomalies are needed in the future.

Here, we do not deny the anthropogenic impact on the SAT extremes, but its direct thermal effect has less impact on the Sum due to its equivalent effect on the increase in warm extremes and the decrease in cold extremes. In addition, we did not rule out the possibility that the AMOC changes were caused by human-induced global warming. More analyses will be carried out to understand how large-scale climate variability interacts with local-scale feedbacks and their mutual effect on regional SAT extremes.

METHODS

Warm and cold extremes
Daily mean SATs during 1960–2017 from the BEST dataset (http://berkeleyearth.org/data/)[61] with a horizontal resolution of 1° × 1° were used to identify the extreme SAT events. Wintertime in this study was defined from November in the current year to February in the next year. February 29 was excluded, and thus, there were 57 winters in our study (the winter of 2017 was excluded due to the lack of data in 2018).

Classical SAT extremes are described by the ETCCDI, where a cold (warm) extreme is identified if the SAT anomaly falls below the 10th percentile (lies above the 90th percentile) of the SAT distribution defined by all 5-day intervals from 1981 to 2010 centred on each calendar day. A new definition based on the ETCCDI procedure but aimed more specifically at regional consistencies was made in this study. For each day within a specific winter month, if more than 50% of the grids in Siberia are characterized by the daily SAT anomalies lying above (falling

below) one (one negative) standard deviation of this month, and among these grids, there are more than 70% grids with SAT anomalies above 1.28 (below −1.28) standard deviation, then an extreme warm (cold) day is identified. Next, we count the frequencies of the warm (cold) extremes in the four months of each winter and isolate the decadal time series by calculating a 9-year moving average.

Composite distributions of the SAT anomalies in winter exhibit regional consistency over Siberia for the occurrences of extremes (see Supplementary Figure 12), which validates the feasibility of our definition. When warm extremes occur (Supplementary Figure 12a), significant positive SAT anomalies are demonstrated over mid- to high latitudes with a maximum changing amplitude of more than 7 K over Siberia. An opposite spatial characteristic is shown with a maximum changing amplitude exceeding −7 K occupying Siberia for cold extremes (Supplementary Figure 12b).

AMOC indices
Two AMOC definitions were chosen for the robustness of the results in the observation. One is the fingerprint index[62] from 1960 to 2017 obtained from http://www.pik-potsdam.de/~caesar/AMOC_slowdown/. The other is the subpolar upper ocean salinity index defined as the average over 45°–65°N in the Atlantic basin and integrated over 0–1500 m (derived from ref. [63]) based on distinct datasets. Additional maximum Atlantic meridional overturning stream functions (known as the max AMOC index) in CMIP6 models are defined as the maximum value at 27.5°N (closest to RAPID 26.5°N at a 2.5° × 2.5° resolution) of the following function:

$$\varphi(z, lat) = \int_z^0 \int_{\lambda_E}^{\lambda_W} V \cos(lat) \, dx \, dz \qquad (1)$$

where $\varphi(z, lat)$ is the Atlantic meridional overturning stream function, V is the meridional velocity, z is the depth, x is the meridional coordinate, and λ_W and λ_E are the west and east boundaries of the Atlantic Basin.

CMIP6 model simulations
Four CMIP6 experiments (https://esgf-node.llnl.gov/projects/cmip6/) are utilized in this study. The historical experiment with a total of 341 members from 44 models is an all-forcing simulation of the recent past based on different realizations (r), initialization (i) schemes, physics (p), and forcing (f) indices[64]. The hist-nat experiment, including 47 members of 10 models, resembles the historical simulations but instead is forced with only solar and volcanic forcing[65]. The hist-GHG experiment with 40 members of 11 models resembles the historical simulations but instead is forced by only well-mixed greenhouse gas changes. Time-varying global annual mean concentrations for long-lived greenhouse gases, including CH_4, N_2O, HFC_s, PFC_s, SF_6, several ODS, and NF_3, serve as inputs[66]. The hist-resAMO experiment, containing 3 members of 3 models, is initialized from the historical run year 1870 and integrated up to the year 2014 with historical forcings and is a pacemaker-coupled historical climate simulation that includes all forcings but with SST restored to the model climatology plus observational historical anomaly in the AMO domain (0–70°N, 70°W–0°) using the same model resolutions as the CMIP6 historical simulation[67]. All these model details are shown in Supplementary Table 2.

Daily near-surface air temperature (tas outputs) was derived from the four experiments. The time lengths for the historical, hist-GHG and hist-nat experiments are 1850–2014 and 1870–2014 for the hist-resAMO experiment. The monthly sea water salinity (so outputs) and sea water meridional velocity (vo outputs) of the FGOALS-f3-L model in the historical experiment and all models in

the hist-resAMO experiment were utilized to calculate the AMOC subpolar upper ocean salinity indices and max AMOC indices, respectively.

The monthly and daily SATs in the historical runs (taking the r1i1p1f1 member of the MPI-ESM-1-2-HAM model for example, which has both daily and monthly tas outputs) were compared to confirm that the temporal resolutions make no difference for an individual member of a particular model. The results are shown in Supplementary Figure 13. Utilizing identical time series makes it possible to analyse the relationship between AMOC derived from the monthly datasets and SAT extremes derived from the daily datasets of the same member of a given model.

Multi-model means are calculated as multi-institution means after performing multi-model means of the same institution. All the model results were interpolated to a resolution of $2.5° \times 2.5°$.

Significance test

We conducted a 9-year running mean to represent the decadal variation in the SAT extremes over Siberia. This may reduce the effective degree of freedom (EDF) when calculating the statistical significance of the correlation coefficients. Thus, in this paper, EDF is estimated via the following equation[68].

$$\frac{1}{N^*} \approx \frac{1}{N} + \frac{2}{N}\sum_{j=1}^{N-2}\frac{N-j}{N}\beta xx(j)\beta yy(j) \quad (2)$$

where N is the sample size and $\beta xx(j)$ and $\beta yy(j)$ are the autocorrelation coefficients of the two time series at lag j.

Other reanalysis variables for the atmosphere and ocean

Six-hourly SAT and Z500 and Z200 are provided by the JRA-55 datasets. Additional daily Z500 and Z200 datasets are derived from the NCEP datasets[69]. Monthly mean horizontal wind velocities at 500 hPa and 200 hPa from the JRA55 and NCEP datasets are used for comparison. The horizontal resolutions for these datasets are $2.5° \times 2.5°$.

Monthly upwards sensible and latent heat fluxes over the global ocean are provided by the WHOI air-sea fluxes for the Global Oceans[70]. Global OHC data at 0–700 m in winter are extracted from the NCEI world ocean heat content dataset[71]. The horizontal resolutions are $1° \times 1°$ for WHOI and $2.5° \times 2.5°$ for NCEI.

The time spans of all the reanalysis datasets are from 1960 to 2017, and all the variables are interpolated into grids of $2.5° \times 2.5°$.

DATA AVAILABILITY

Daily mean SATs are from the BEST dataset (http://berkeleyearth.org/data/). The fingerprint index of AMOC was obtained from (http://www.pik-potsdam.de/~caesar/AMOC_slowdown/). CMIP6 simulation results were obtained from https://esgf-node.llnl.gov/projects/cmip6/. The JRA-55 and NECP reanalysis datasets are available at https://rda.ucar.edu/datasets/ds628.0/ and https://psl.noaa.gov/data/gridded/data.ncep.reanalysis.html, respectively. Monthly surface heat fluxes over the global ocean are provided by the WHOI (https://oaflux.whoi.edu/data-access/). 0–700 m global OHC extracted from NCEI is from https://www.ncei.noaa.gov/access/global-ocean-heat-content/. All relevant data and source codes are available from the corresponding author upon reasonable request.

REFERENCES

1. Donat, M. G., Alexander, L. V., Herold, N. & Dittus, A. J. Temperature and precipitation extremes in century-long gridded observations, reanalyses, and atmospheric model simulations. J. Geophys. Res. Atmos. **121**, 11174–11189 (2016).
2. Dunn, R. J. H. et al. Development of an updated global land in-situ-based dataset of temperature and precipitation extremes: HadEX3. J. Geophys. Res. Atmos. **125**, 1–28 (2020).
3. Zhang, P. et al. Observed changes in extreme temperature over the global land based on a newly developed station daily dataset. J. Clim. **32**, 8489–8509 (2019).
4. Zhang, M., Chen, Y., Shen, Y. & Li, B. Tracking climate change in Central Asia through temperature and precipitation extremes. J. Geogr. Sci. **29**, 3–28 (2019).
5. Almazroui, M. et al. Projected changes in climate extremes using CMIP6 simulations Over SREX regions. Environ. Earth Sci. **5**, 481–497 (2021).
6. Cohen, J. L. et al. Arctic warming, increasing snow cover and widespread boreal winter cooling. Environ. Res. Lett. **7**, 14007–14014 (2012).
7. Wegmann, M., Orsolini, Y. & Zolina, O. Warm Arcticcold Siberia: comparing the recent and the early 20th-century Arctic warmings. Environ. Res. Lett. **13**, 025009 (2018).
8. Petoukhov, V. & Semenov, V. A. A link between reduced Barents-Kara sea ice and cold winter extremes over northern continents. J. Geophys. Res. Atmos. **115**, D21111 (2010).
9. Cattiaux, J. R. et al. Winter 2010 in Europe: A cold extreme in a warming climate. Geophys. Res. Lett. **37**, 114–122 (2010).
10. Christiansen, B. et al. Was the cold European winter 2009-2010 modified by anthropogenic climate change? An attribution study. J. Clim. **31**, 3387–3410 (2018).
11. Overland, J. E., Wood, K. R. & Wang, M. Warm Arctic–cold continents: climate impacts of the newly open Arctic sea. Polar Res **30**, 15787 (2011).
12. Cohen, J. et al. Divergent consensuses on Arctic amplification influence on mid-latitude severe winter weather. Nat. Clim. Chang. **10**, 20–29 (2020).
13. Overland, J. E. et al. How do intermittency and simultaneous processes obfuscate the Arctic influence on midlatitude winter extreme weather events? Environ. Res. Lett. **16**, 043002 (2021).
14. Screen, J. A. & Simmonds, I. Amplified mid-latitude planetary waves favour particular regional weather extremes. Nat. Clim. Chang. **4**, 704–709 (2014).
15. Seneviratne, S. I. et al. Weather and Climate Extreme Events in a Changing Climate. (Cambridge Univ. Press, 2021).
16. Jin, C. H., Wang, B., Yang, Y. M. & Liu, J. "Warm Arctic-cold Siberia" as an internal mode instigated by North Atlantic warming. Geophys. Res. Lett. **47**, e2019GL086248 (2020).
17. Bonnet, R. et al. Increased risk of near term global warming due to a recent AMOC weakening. Nat. Commun. **12**, 6108 (2021).
18. Johnson, N. C., Xie, S. P., Kosaka, Y. & Li, X. Increasing occurrence of cold and warm extremes during the recent global warming slowdown. Nat. Commun. **9**, 1724 (2018).
19. Knight, J. R., Folland, C. K. & Scaife, A. A. Climate impacts of the Atlantic multi-decadal oscillation. Geophys. Res. Lett. **33**, L17706 (2006).
20. Mahajan, S., Zhang, R. & Delworth, T. L. Impact of the Atlantic Meridional Overturning Circulation (AMOC) on Arctic Surface Air Temperature and Sea Ice Variability. J. Clim. **24**, 6573–6581 (2011).
21. Sutton, R. T. & Hodson, D. Atlantic Ocean forcing of North American and European summer climate. Science **309**, 115–118 (2005).
22. Liu, W., Fedorov, A. V., Xie, S. P. & Hu, S. Climate impacts of a weakened Atlantic Meridional Overturning Circulation in a warming climate. Sci. Adv. **6**, eaaz4876 (2020).
23. Trenberth, K. E. & Fasullo, J. T. Atlantic meridional heat transports computed from balancing Earth's energy locally. Geophys. Res. Lett. **44**, 1919–1927 (2017).
24. Zuo, Z., Li, M., An, N. & Xiao, D. Variations of widespread extreme cold and warm days in winter over China and their possible causes. Sci. China Earth Sci. **65**, 337–350 (2022).
25. Ganachaud, A. & Wunsch, C. Improved estimates of global ocean circulation, heat transport and mixing from hydrographic data. Nature **408**, 453 (2000).
26. Delworth, T. L. et al. The North Atlantic Oscillation as a driver of rapid climate change in the Northern Hemisphere. Nat. Geosci. **9**, 509–513 (2016).
27. Spielhagen, R. F. et al. Enhanced modern heat transfer to the arctic by warm Atlantic water. Science **331**, 450–453 (2011).
28. Screen, J. A. & Simmonds, I. The central role of diminishing sea ice in recent Arctic temperature amplification. Nature **464**, 1334–1337 (2010).
29. Barnes, E. A., Dunn-Sigouin, E., Masato, G. & Woollings, T. Exploring recent trends in Northern Hemisphere blocking. Geophys. Res. Lett. **41**, 638–644 (2014).
30. Sun, L., Perlwitz, J. & Hoerling, M. What caused the recent "Warm Arctic, Cold Continents" trend pattern in winter temperatures? Geophys. Res. Lett. **43**, 5345–5352 (2016).
31. Jarque, C. M. Jarque-Bera Test (Springer Berlin Heidelberg, 2011).
32. Alexander, L. V. et al. Global observed changes in daily climate extremes of temperature and precipitation. J. Geophys. Res. Atmos. **111**, D05109 (2006).
33. Ebita, A. et al. The Japanese 55-year reanalysis "JRA-55": An Interim Report. SOLA **7**, 149–152 (2011).

34. Fischer, E., Sedlacek, J., Hawkins, E. & Knutti, R. Models agree on forced response pattern of precipitation and temperature extremes. *Geophys. Res. Lett.* **41**, 8554–8562 (2014).

35. Li, C. et al. Changes in annual extremes of daily temperature and precipitation in CMIP6 models. *J. Clim.* **34**, 1–61 (2020).

36. Zwiers, F. W., Zhang, X. & Yang, F. Anthropogenic influence on long return period daily temperature extremes at regional scales. *J. Clim.* **24**, 881–892 (2011).

37. Catalano, A. J., Loikith, P. C. & Neelin, J. D. Evaluating CMIP6 model fidelity at simulating non-Gaussian temperature distribution tails. *Environ. Res. Lett.* **15**, 074026 (2020).

38. Huang, X. et al. The recent decline and recovery of Indian summer monsoon rainfall: relative roles of external forcing and internal variability. *J. Clim.* **33**, 5035–5060 (2020).

39. Dai, A., Fyfe, J. C., Xie, S. P. & Dai, X. Decadal modulation of global surface temperature by internal climate variability. *Nat. Clim. Chang.* **5**, 555–559 (2015).

40. Delsole, T., Tippett, M. K. & Shukla, J. A significant component of unforced multidecadal variability in the recent acceleration of global warming. *J. Clim.* **24**, 909–926 (2011).

41. Knight, J. R. et al. A signature of persistent natural thermohaline circulation cycles in observed climate. *Geophys. Res. Lett.* **32**, L20708 (2005).

42. McCarthy, G. et al. Observed interannual variability of the Atlantic Meridional Overturning Circulation at 26.5°N. *Geophys. Res. Lett.* **39**, 19609 (2012).

43. Danabasoglu, G. et al. North Atlantic simulations in Coordinated Ocean-ice Reference Experiments phase II (CORE-II). Part I: Mean states. *Ocean Model* **73**, 76–107 (2014).

44. Weijer, W. et al. CMIP6 models predict significant 21st century decline of the Atlantic Meridional Overturning Circulation. *Geophys. Res. Lett.* **47**, (2020).

45. Bryan, K. Measurements of meridional heat transport by ocean currents. *J. Geophys. Res.* **67**, 3403–3414 (1962).

46. Takaya, K. & Nakamura, H. A. Formulation of a phase-independent wave-activity flux for stationary and migratory quasigeostrophic eddies on a zonally varying basic flow. *J. At. Sci.* **58**, 608–627 (2001).

47. Yao, Y., Luo, D., Dai, A. & Simmonds, I. Increased quasi stationarity and persistence of winter Ural blocking and Eurasian extreme cold events in response to Arctic warming. Part I: Insights from observational analyses. *J. Clim.* **23**, 8027–8046 (2017).

48. Ma, S. & Zhu, C. Opposing trends of winter cold extremes over Eastern Eurasia and North America under recent Arctic warming. *Adv. Atmos. Sci.* **37**, 1417–1434 (2020).

49. Horton, D. E. et al. Contribution of changes in atmospheric circulation patterns to extreme temperature trends. *Nature* **522**, 465–469 (2015).

50. Brunner, L. et al. Dependence of present and future European temperature extremes on the location of atmospheric blocking. *Geophys. Res. Lett.* **45**, 077837 (2018).

51. Kornhuber, K. et al. Amplified Rossby waves enhance risk of concurrent heatwaves in major breadbasket regions. *Nat. Clim. Chang.* **10**, 1–6 (2020).

52. Schaller, N. et al. Influence of blocking on Northern European and Western Russian heatwaves in large climate model ensembles. *Environ. Res. Lett.* **13**, 054015 (2018).

53. Chen, R., Wen, Z. & Lu, R. Evolutions of the circulation anomalies and the quasi-biweekly oscillations associated with extreme heat events in South China. *J. Clim.* **29**, 6909–6921 (2016).

54. Rohini, P., Rajeevan, M. & Srivastava, A. K. On the variability and increasing trends of heat waves over India. *Sci. Rep.* **6**, 26153 (2016).

55. You, Q. et al. Warming amplification over the Arctic Pole and Third Pole: trends, mechanisms and consequences. *Earth Sci. Rev.* **217**, 103625 (2021).

56. Francis, J. A. & Vavrus, S. J. Evidence linking Arctic amplification to extreme weather in mid-latitudes. *Geophys. Res. Lett.* **39**, l06801 (2012).

57. Liu, J. et al. Impact of declining Arctic sea ice on winter snowfall. *Proc. Natl Acad. Sci. USA* **109**, 4074–4079 (2012).

58. Shepherd, T. G. A common framework for approaches to extreme event attribution. *Curr. Clim. Change Rep.* **2**, 28–38 (2016).

59. Cohen, J. et al. Recent Arctic amplification and extreme mid-latitude weather. *Nat. Geosci.* **7**, 627–637 (2014).

60. Renssen, H. et al. Multiple causes of the Younger Dryas cold period. *Nat. Geosci.* **8**, 946–949 (2015).

61. Rohde, R. A. & Hausfather, Z. The Berkeley Earth land/ocean temperature record. *Earth Syst. Sci. Data* **12**, 3469–3479 (2020).

62. Caesar, L. et al. Observed fingerprint of a weakening Atlantic Ocean overturning circulation. *Nature* **556**, 191 (2018).

63. Chen, X. & Tung, K.-K. Global surface warming enhanced by weak Atlantic overturning circulation. *Nature* **559**, 387–391 (2018).

64. Veronika, E. et al. Overview of the Coupled Model Intercomparison Project Phase 6 (CMIP6) experimental design and organization. *Geosci. Model. Dev.* **9**, 1937–1958 (2016).

65. Gillett, N. P. et al. The Detection and Attribution Model Intercomparison Project (DAMIP v1.0) contribution to CMIP6. *Geosci. Model Dev.* **9**, 3685–3697 (2016).

66. Meinshausen, M. et al. Historical greenhouse gas concentrations for climate modelling (CMIP6). *Geosci. Model. Dev.* **10**, 2057–2116 (2017).

67. Enfield, D., Mestas-Nunez, A. & Trimble, P. The Atlantic multidecadal oscillation and its relation to rainfall and river flows in the continental US. *Geophys. Res. Lett.* **28**, 2077–2080 (2001).

68. Zhao, W. & Khalil, M. The relationship between precipitation and temperature over the contiguous United States. *J. Clim.* **6**, 1232–1236 (1993).

69. Kalnay, E. et al. The NCEP/NCAR 40-year reanalysis project. *Bull. Am. Meteorol. Soc.* **77**, 437–472 (1996).

70. Yu, L., Jin, X. & Weller, R. A. *Multidecade Global Flux Datasets from the Objectively Analyzed Air-sea Fluxes (OAFlux) Project: Latent and Sensible Heat Fluxes, Ocean Evaporation, and Related Surface Meteorological Variables* (OAFlux Project Technical Report OA-2008-01, Woods Hole, 2008).

71. Chu, P. C. & Fan, C. Global ocean synoptic thermocline gradient, isothermal-layer depth, and other upper ocean parameters. *Sci. Data* **6**, 119 (2019).

AUTHOR CONTRIBUTIONS

Huan Wang and Zhiyan Zuo contributed to designing the study, conducting the analyses and writing the paper. Liang Qiao and Kaiwen Zhang contributed to conceiving the study and analysing the CMIP6 model data. Cheng Sun and Dong Xiao contributed to conceiving the experiments and interpreting the results. Zouxing Lin, Lulei Bu and Ruonan Zhang contributed to writing this manuscript.

COMPETING INTERESTS

The authors declare no competing interests.

ADDITIONAL INFORMATION

Supplementary information The online version contains supplementary material available at https://doi.org/10.1038/s41612-022-00307-w.

Correspondence and requests for materials should be addressed to Zhiyan Zuo.

Reprints and permission information is available at http://www.nature.com/reprints

Publisher's note Springer Nature remains neutral with regard to jurisdictional claims in published maps and institutional affiliations.